

MIT Open Access Articles

Nanoscale transient gratings excited and probed by extreme ultraviolet femtosecond pulses

The MIT Faculty has made this article openly available. **Please share** how this access benefits you. Your story matters.

Citation: Bencivenga, F. et al. "Nanoscale transient gratings excited and probed by extreme ultraviolet femtosecond pulses." *Science Advances* 5, 7 (July 2019): eaaw5805 © 2019 The Author(s)

As Published: <http://dx.doi.org/10.1126/sciadv.aaw5805>

Publisher: American Association for the Advancement of Science (AAAS)

Persistent URL: <https://hdl.handle.net/1721.1/123524>

Version: Final published version: final published article, as it appeared in a journal, conference proceedings, or other formally published context

Terms of use: Creative Commons Attribution NonCommercial License 4.0



OPTICS

Nanoscale transient gratings excited and probed by extreme ultraviolet femtosecond pulses

F. Bencivenga^{1*}, R. Mincigrucci¹, F. Capotondi¹, L. Foglia¹, D. Naumenko¹, A. A. Maznev², E. Pedersoli¹, A. Simoncig¹, F. Caporaletti³, V. Chiloyan², R. Cucini⁴, F. Dallari³, R. A. Duncan², T. D. Frazer⁵, G. Gaio¹, A. Gessini¹, L. Giannessi¹, S. Huberman², H. Kapteyn⁵, J. Knobloch⁵, G. Kurdi¹, N. Mahne^{1,4}, M. Manfredda¹, A. Martinelli³, M. Murnane⁵, E. Principi¹, L. Raimondi¹, S. Spampinati¹, C. Spezzani¹, M. Trovò¹, M. Zangrando^{1,4}, G. Chen², G. Monaco³, K. A. Nelson², C. Masciovecchio^{1*}

Copyright © 2019
The Authors, some
rights reserved;
exclusive licensee
American Association
for the Advancement
of Science. No claim to
original U.S. Government
Works. Distributed
under a Creative
Commons Attribution
NonCommercial
License 4.0 (CC BY-NC).

Advances in developing ultrafast coherent sources operating at extreme ultraviolet (EUV) and x-ray wavelengths allows the extension of nonlinear optical techniques to shorter wavelengths. Here, we describe EUV transient grating spectroscopy, in which two crossed femtosecond EUV pulses produce spatially periodic nanoscale excitations in the sample and their dynamics is probed via diffraction of a third time-delayed EUV pulse. The use of radiation with wavelengths down to 13.3 nm allowed us to produce transient gratings with periods as short as 28 nm and observe thermal and coherent phonon dynamics in crystalline silicon and amorphous silicon nitride. This approach allows measurements of thermal transport on the ~10-nm scale, where the two samples show different heat transport regimes, and can be applied to study other phenomena showing nontrivial behaviors at the nanoscale, such as structural relaxations in complex liquids and ultrafast magnetic dynamics.

INTRODUCTION

The invention of the laser, a high-brightness source of coherent light, gave rise to the field of nonlinear optics, with a plethora of nonlinear optical techniques devised and applied to a wide range of problems in science. The recent development of free electron lasers (FELs) now allows us to push nonlinear optics toward shorter wavelengths, from extreme ultraviolet (EUV) to hard x-rays (1–4). One fundamental nonlinear process is four wave mixing (FWM), in which three optical fields are brought into interaction in a sample to generate a fourth one. The laser-induced transient grating (TG) technique is a variation of noncollinear FWM, in which two short optical pulses of the same wavelength are overlapped in time and space in the sample to produce a spatially periodic material excitation that is probed via diffraction of a third variably delayed pulse. TG spectroscopy is used to study a wide range of phenomena in condensed matter such as the propagation of acoustic waves (5, 6) and phonon polaritons (7), thermal transport (8, 9), molecular diffusion (10), carrier and spin dynamics (11, 12), magnetic recording (13), charge density waves (14), laser-plasma interaction (15), and dynamical behavior of proteins (16). It is also widely used in materials science for noncontact characterization of elastic and thermal properties. However, the potential of the TG technique for studying nanoscale phenomena has been limited by the fact that the TG period (L_{TG}) has a lower bound at $\lambda_{ex}/2$, where λ_{ex} is the excitation wavelength. The use of short wavelengths will greatly expand the capabilities of the TG spectroscopy by allowing to probe high-wave vector excitations and to study transport phenomena on the nanoscale.

Recent studies conducted at the Free Electron Laser Radiation for Multidisciplinary Investigations (FERMI FEL) [Trieste, Italy (17)] dem-

onstrated TGs excited by femtosecond EUV pulses with wavelengths in the 13- to 30-nm range and probed by an optical pulse (4, 18). However, the optical probing limited the range of TG periods to above $\lambda_{pr}/2$, where λ_{pr} is the probe wavelength. TGs with shorter periods could be generated by FEL pulses but would be “invisible” to the optical probe because gratings with periods shorter than one-half the wavelength cannot produce diffraction. This limitation can be overcome by introducing a third, noncollinear, and time-delayed EUV pulse derived from the same FEL source to probe the induced dynamics. The first step toward the EUV probe was made in a study (19) where the diffraction of copropagating and time-coincident FEL harmonics by a TG generated by the fundamental FEL radiation was observed. However, a variably delayed EUV probe pulse is needed to study TG-induced dynamics.

Here, we report the first EUV pump/EUV probe TG (EUV TG) measurements and demonstrate vibrational and thermal lattice responses in silicon and silicon nitride at L_{TG} 's down to 28 nm. The EUV TG capability has been implemented in the TIMER beamline (20) at the FERMI FEL. Our results reveal thermal transport kinetics that can now be studied incisively, and we discuss the potential of this new class of experiments for studying structural dynamics, transport phenomena, and magnetism on the nanoscale.

RESULTS

The experimental setup is sketched in Fig. 1A. The output of the FEL source [40- to 70-fs EUV pulse with high transverse and longitudinal coherence (17)] is split by a wavefront division beam splitter into excitation and probe beams. The former is further split into two excitation beams (see Fig. 1, B and C) that are then focused and overlapped at the sample to generate a TG with spatial periodicity $L_{TG} = \lambda_{ex}/2\sin(\theta)$, where 2θ is the crossing angle between the excitation pulses. In the present experiment, 2θ was fixed to 27.6°, while λ_{ex} was varied in the 54- to 13.3-nm range to change the periodicity of the EUV excitation pattern; used values of L_{TG} were 110, 85, and 28 nm. Because the seeded FEL pulses from FERMI are nearly transform limited, the crossed excitation pulses yield a high-contrast interference

¹ Elettra Sincrotrone Trieste S.C.p.A., Strada Statale 14, km 163.5, 34149 Basovizza (TS), Italy. ² Massachusetts Institute of Technology, 77 Massachusetts Avenue, Cambridge, MA 02139, USA. ³ Department of Physics, University of Trento, Via Sommarive 14, Povo (TN), Italy. ⁴ IOM-CNR, Strada Statale 14, km 163.5, in Area Science Park, I-34012 Basovizza (TS), Italy. ⁵ JILA and Department of Physics, University of Colorado, Boulder, CO 80309, USA.

*Corresponding author. Email: filippo.bencivenga@elettra.eu (F.B.); claudio.masciovecchio@elettra.eu (C.M.)

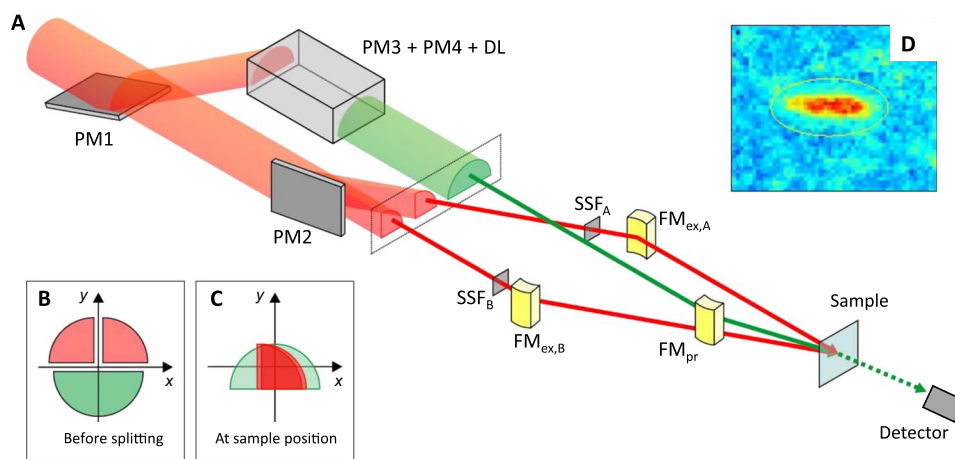


Fig. 1. Experimental setup. The setup used in the present experiment is schematically shown in (A). The red beams are the excitation pulses (λ_{ex}), while the green one is the probe (λ_{pr}). The green dashed line downstream is the signal beam. PM1 is a plane mirror used to route half of the beam into the probe's branch line. The latter consists of two additional plane mirrors (PM3 and PM4) and a DL, made out by four multilayer mirrors (not shown) with high reflectivity at λ_{pr} ; the DL thus also acts as a bandpass filter at λ_{pr} . The radiation at λ_{pr} in the branch lines of the excitation pulses is removed by SSFs (SSF_A and SSF_B). The three beams are finally focused at the sample at the desired angles by three focusing mirrors (FM). (B and C) Sketch of the wavefront division beam-splitting approach. (D) Image of the signal beam on the detector.

pattern extending up to several tens of micrometers, nearly matching the $\sim 100\text{-}\mu\text{m}$ beam spot size. The EUV probe pulse is routed into a delay line (DL) that controls the time delay (Δt) with respect to the TG excitation and whose transmission acts as a bandpass filter at λ_{pr} . The probe beam is then focused and spatially overlapped with the excitation beams at the sample. The FEL output contains both the fundamental and high harmonics [as well as the fundamental output of the first amplification stage when a double cascade FEL generation scheme is used (17)], and therefore, the excitation and probe wavelengths can be either the same or different, depending on filtering after the splitting. The diffracted probe pulse is detected in transmission geometry and has the shape of a well-defined beam (see Fig. 1D), containing some tens of photons/shot. The signal was averaged over a few thousand shots for each value of Δt , and the FEL repetition rate was 50 Hz. The samples were amorphous silicon nitride (Si_3N_4) and crystalline silicon (Si) membranes. Additional details on the experiment are shown in Materials and Methods.

Figure 2 displays the EUV TG signal intensity from Si_3N_4 as a function of Δt at different values of L_{TG} . At negative delays, the signal is absent because there is no grating in the sample to diffract the probe beam. The signal appears after $\Delta t = 0$ and exhibits a slowly decaying component with modulations, matching the frequency of the longitudinal acoustic waves at the wavelength L_{TG} . In contrast with experiments with optical probing (4, 18), where the rise time of the signal at $\Delta t = 0$ was about equal to the pulse duration, here, the signal rise is slower and depends on L_{TG} . The maximum signal is delayed by one-half of the acoustic oscillations period, indicating that the dominant contribution to the signal originates from density changes. The slow decaying component can then be ascribed to a “thermal grating,” produced by thermal expansion, modulated by the coherent phonon dynamics and decaying via thermal transport (8, 18, 21). Both the slow signal decay (red lines in Fig. 2) and the apparent decay of the oscillations are thus related to the thermal equilibration time (τ_{th}). While the coherent phonon dynamics can decay with a different time scale and persist beyond τ_{th} (18), the present data do not allow us to investigate this behavior in detail (see Materials and Methods).

An evident feature of the signal is the almost complete absence of the so-called electronic peak at time zero, when the excitation and probe pulses overlap, which is usually the most intense feature observed in optically probed EUV TG experiments (4, 18). In the data shown in Fig. 2D, this is barely perceivable as a bump (enclosed in the red circle and poorly resolved due to the $\sim 150\text{-fs}$ Δt sampling) on top of the rising edge of the first acoustic oscillation. This behavior is not unexpected, as also observed in EUV-probed optical TG experiments from metallic surfaces (22), and reflects the fact that the refraction index changes at optical wavelengths are highly sensitive to electronic excitations in the conduction/valence band, while at EUV wavelengths, they are mostly sensitive to changes in the total electronic density. Thus, the EUV TG signal is dominated by the lattice response.

Figure 3A shows the oscillation frequency ν , extracted from a Fourier transform of the signal waveform after subtraction of the slow decay, as a function of the wave vector $2\pi/L_{TG}$. The expected linear dependence yields a slope that matches the group velocity ($c = \nu L_{TG} = 10.3 \pm 0.3$ km/s) of longitudinal acoustic phonons (23). Figure 3B displays the thermal relaxation rate $\tau_{th}^{-1} = \tau^{-1}/2$, where τ is the decay time obtained by fitting the data by an exponential function (the factor 1/2 results from the fact that the diffraction signal is proportional to the square of the density grating amplitude). The data fit very well to a quadratic dependence of τ_{th}^{-1} on $2\pi/L_{TG}$, as expected for thermal transport in the diffusive regime (8, 18, 21), with a diffusion coefficient $D_T = \tau_{th}^{-1} L_{TG}^2 / 4\pi^2 = 470 \pm 90$ nm²/ns that is consistent with the literature data (24). Further details on the data analysis are reported in Materials and Methods.

Figure 4 displays the EUV TG signal from Si at $L_{TG} = 110$ nm, while the inset shows the region close to $\Delta t = 0$ sampled with 50-fs steps in Δt , confirming the weakness of the electronic response. The oscillation frequency, $\nu = 75 \pm 2$ GHz, is in line with the expected longitudinal sound frequency at the TG wavelength. In contrast, the observed thermal decay is much slower than the prediction of the thermal diffusion model, shown by the blue line in Fig. 4. The measured value of $\tau_{th} = 73 \pm 12$ ps is more than one order of magnitude longer than the decay time calculated from the thermal diffusivity of Si, i.e., 3.9 ps, resulting into an effective thermal conductivity

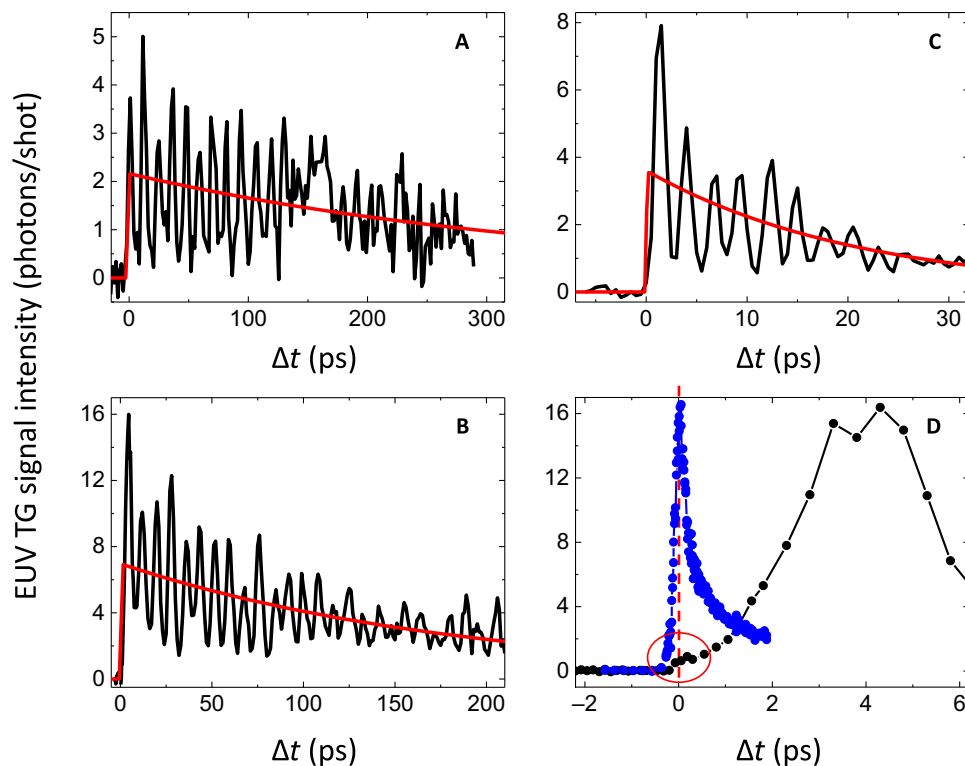


Fig. 2. EUV TG signal. Black lines in (A), (B), and (C) are the EUV TG signals from Si_3N_4 membranes at $L_{\text{TG}} = 110$, 85, and 28 nm, respectively, while the red line through the data is an exponential decay that accounts for the overall signal decay. (D) Comparison of the EUV TG signal at $L_{\text{TG}} = 85$ nm, sampled with finer steps around the time zero region (black circles connected by lines), with the optically probed EUV TG signal (blue circles connected by lines; in this case, $L_{\text{TG}} = 280$ nm and the sample is a 500-nm-thick Si_3N_4 membrane); the latter data are scaled to fit in the same scale, the vertical red dashed line indicates $\Delta t = 0$, while the red circle encloses the small bump observed at time zero in the EUV TG data.

$k_{\text{eff}} = L_{\text{TG}}^2 \rho C / 4\pi^2 \tau_{\text{th}} \sim 8 \text{ W m}^{-1} \text{ K}^{-1}$ (with ρ as the density and C as the specific heat) against a bulk value at room temperature of $150 \text{ W m}^{-1} \text{ K}^{-1}$. In Si, at this length scale, the thermal diffusion model yields an unreasonable result, because the predicted thermal decay time would be shorter than an acoustic cycle, hence implying that heat propagates faster than longitudinal phonons (i.e., the fastest heat carriers). Evidently, the observed heat transport is very far from the diffusive regime, although the ballistic limit is not yet achieved, as the observed thermal decay is still substantially slower than the acoustic wave period.

DISCUSSION

We have demonstrated the capability to generate nanoscale TGs and probe their dynamics in the time domain using noncollinear FEL pulses. The extension to single-digit nanometer TG periodicities is within reach with the present setup by exploiting larger crossing angles and shorter wavelengths. EUV TG experiments will open multiple avenues for studying condensed matter dynamics.

In one aspect, we have demonstrated Brillouin light scattering in the EUV range. While Brillouin scattering of visible and x-ray photons (as well as neutrons) are well-established experimental tools, EUV Brillouin scattering has not been observed because of the lack of EUV spectrometers with high enough spectral resolution (an additional complication being the small scattering volume due to the short absorption length). In the EUV TG approach, this difficulty is circumvented by using stimulated scattering by coherent phonons produced by the excitation pulses and detecting the signal in the time

domain. Furthermore, as a time domain technique, it is not subject to limitations due to the instrumental spectral resolution and is advantageous for probing overdamped phonon modes, which may not show up as distinct peaks in the spectra (25). EUV TG can thus fill the wavelength gap between optical and x-ray/neutron Brillouin scattering (26, 27). The access to these mesoscopic (tens of nanometer) length scales is particularly beneficial for studying structural dynamics in systems without translational invariance, such as liquids and glasses. For instance, the behavior of phonons at a few nanometers wavelength, i.e., on length scales comparable to the postulated spatial fluctuations in the elastic moduli, could be the key for setting long-standing issues related to the thermal behavior of glasses with respect to their crystalline counterparts (28, 29). Another important problem that can be addressed by EUV TG is that of mesoscopic structural dynamics of the hydrogen bond network in water, which is expected to hold information on the remarkable thermodynamic anomalies displayed by this liquid (26, 30). These mesoscopic structural dynamics are also of primary interest for chemical and biological systems, ranging from ionic liquids to gels to biopolymers, and their interactions with aqueous environments. In this context, the concurrent development of ultrafast electron microscopy techniques for studying coherent phonons at the nanoscale is worth mentioning (31, 32). While the use of FEL pulses in a EUV TG scheme warrants higher time resolution and wave vector selectivity in a broad range, the shorter De Broglie wavelength of 100's keV electrons provides higher spatial resolution. One can thus envision combining EUV TG excitation with a time-resolved electron microscopy probe that

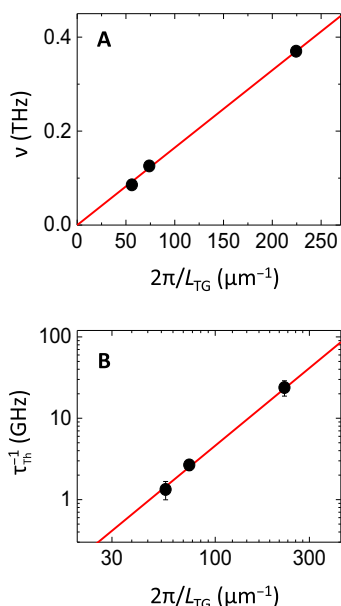


Fig. 3. Dispersion of EUV TG signal parameters. Full dots are the dispersion relations of the frequency (A) and decay rate (B) as a function of the EUV TG wave vector ($2\pi/L_{TG}$), as extracted from the data shown in Fig. 2. Red lines indicate the linear and quadratic trends of these two quantities.

would take advantage of the wave vector selectivity in the broad range of the former and the superior spatial resolution of the latter.

In another aspect, EUV TG will help to advance studies of nanoscale transport phenomena. For instance, measurements of heat transport over nanoscale distances are currently done with the help of fabricated nanostructures (33–35), which complicates the interpretation of the results. In the TG method, the effective heat transfer distance L_{TG}/π is determined by the excitation pattern, with no need for nanofabrication. The weak sensitivity of the EUV TG signal to electronic excitations additionally simplifies the interpretation of the data. In our measurement on Si_3N_4 at $L_{TG} = 28$ nm, the effective heat transport distance is below 10 nm, beyond what is currently possible with nanostructures (33–35). The initial EUV TG measurements reported here already yield valuable information: The quadratic dependence of the thermal decay time on L_{TG} in Si_3N_4 [a material relevant for several nanotechnological applications (35)] indicates that the heat transport is in the diffusive regime; hence, the mean free path of heat carriers is shorter than the few tens of nanometer scale. This observation is in contradiction to an intriguing report (35), which suggests that about half of the heat in Si_3N_4 at room temperature is carried by phonons with mean free paths ~ 1 μm . On the other hand, the remarkable deviation from the diffusive regime observed in Si qualitatively confirms recent results, showing that the Fourier law of heat diffusion fails on the nanoscale, when the heat transfer distance becomes comparable to the phonon mean free path (8, 33–35). Moderate deviations from the diffusive trend have been found in Si at a distance scale of about 1 μm by optical TG (8) and ascribed to the transition toward a ballistic regime of heat propagation. EUV TG experiments allow us to probe thermal transport in a strongly nondiffusive regime. The EUV TG method can then be used to study nondiffusive heat transport in Si and other microelectronic materials on the tens of nanometer length scales, most relevant to state-of-the-art microelectronics.

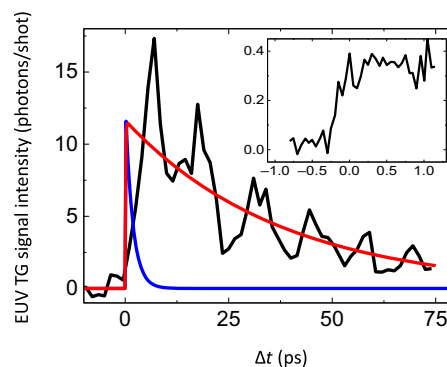


Fig. 4. EUV TG signal from Si. The black line is the EUV TG signal from Si at $L_{TG} = 110$ nm, the red line through the data is an exponential decay that accounts for the overall signal decay, while the blue line is the decay expected according to heat diffusion theory. The inset shows the region close to time zero sampled with finer Δt steps and larger accumulation time to reduce the noise level relative to that in the data shown in the main panel.

Furthermore, we believe that the EUV TG technique also holds great potential for studying nanoscale magnetic phenomena. EUV light at a wavelength tuned to an absorption edge of a magnetic element has already been demonstrated to be a sensitive probe, via magnetic circular dichroism, for ultrafast magnetic phenomena initiated by optical excitation (36). We expect that the same effect will enhance the diffraction efficiency of a magnetization grating produced by EUV TG excitation. Writing magnetic domains using optical TG has just recently been demonstrated (13); the EUV TG technique will allow writing domains as narrow as some nanometers and study of the dynamics of the magnetization switching process. We also envision studying ultrafast spin diffusion over the tens of nanometer scale, as well as the excitation of magnons with wavelength controlled by the TG period; the scattering of EUV light by short-wavelength magnons is yet another unexplored phenomenon that can be studied using the EUV TG approach.

Most generally, the results presented here represent the first time-resolved FWM experiment carried out by exclusively using EUV pulses. The capability to perform these experiments represents an advance in nonlinear optics. These initial data strongly suggest that resonant enhancements of the nonlinear susceptibility (e.g., by tuning the wavelengths of the input field to core-hole excitations) are needed to detect the ultrafast electronic response and would allow the realization of nonlinear spectroscopies of electronic excitations with chemical selectivity (37). These experiments can be exploited in a range of studies, spanning from correlations between core and valence electronic excitations to charge and energy transfer processes between selected atoms in a molecule. As in nonlinear spectroscopy in other spectral ranges, we can envision extension of the current approach to EUV photon echoes, multiple quantum measurements, and coherent multidimensional spectroscopy, including variations that require full-phase coherence among multiple EUV fields.

While we anticipate a number of exciting advancements enabled by the EUV TG technique, other unanticipated developments are likely to emerge. We believe that EUV TG capabilities will be further exploited by a broad cross section of researchers in optics, condensed matter, and materials science. We also expect that the expansion of the TG approach in the hard x-ray range will open further exciting opportunities.

MATERIALS AND METHODS

Optical setup

The optical system for EUV TG experiments presents critical aspects, for instance, the mandatory use of reflective optics, which have required huge technical efforts before making EUV TG experiments a reality; further technical details on the setup can be found elsewhere (20). The three EUV pulses were generated from a single FEL pulse using the edges of two splitting flat mirrors (PM1 and PM2) working in the vertical and horizontal plane, respectively. Half of the FEL pulse wavefront impinging on the edge of PM1 is sent, through two plane mirrors (PM3 and PM4), to a DL consisting of four multilayer-coated mirrors working at a 45° angle of incidence and designed to reflect, with high efficiency, the (vertically polarized) radiation at λ_{pr} , which is used as “probe.” The right-angle design allows the exploitation of a large Δt range (up to a few nanoseconds), which is necessary to detect the relatively slow lattice dynamics, and for compensating the change in the optical path length when 2θ is changed. The beam emerging from the DL was focused by a toroidal FM (FM_{pr}). The half beam not intercepted by PM1 was further split into two halves by PM2, and these two “pump” beams were finally focused by two toroidal FMs (FM_{ex,A} and FM_{ex,B}) to generate the EUV TG. Different pairs of mirrors were used to change the value of 2θ , which was fixed at 27.6° for the present experiment. The two pump beams and the probe one lie on the same (horizontal) plane. The spot size at the sample was about $150 \times 150 \mu\text{m}^2$ for the pump beams and $100 \times 100 \mu\text{m}^2$ for the probe one. The EUV TG signal was detected by an in-vacuum charge-coupled device (CCD) camera (MTE, Princeton Instruments), placed on a translational stage, and positioned along the expected signal direction.

The instrumental design foresees the use of different EUV wavelengths for generating (λ_{ex}) and probing (λ_{pr}) the TG, with $\lambda_{ex}/\lambda_{pr} = 3$. In this case, the optimized phase matching conditions (Bragg scattering) were achieved when the angle of incidence of the probe was $\theta_{pr} = \sin^{-1}[\sin(\theta)/3]$, with the signal beam propagating along $\theta_{sig} = -\theta_{pr}$. The signal was thus emitted in a vastly different direction from those of the (much more intense) input beams that have angular offsets of at least $\pm 2\theta/3$. Such a “background-free” condition is typical of noncollinear wave-mixing experiments, as TG, and is largely favorable in terms of signal-to-noise ratio. The use of two distinct wavelengths also allows us to filter out the spurious scattering from the pump by placing a solid-state filter (SSF) in front of the detector, while two SSFs placed before M_A and M_B (see Fig. 1A) can be used to suppress the FEL radiation at λ_{pr} that propagates collinearly with the two pump pulses. For instance, in fig. S1A, we show the filtering used for acquiring the data reported in Fig. 2B.

Experimental details

The experiment was carried out by keeping θ_{pr} fixed at 4.5° and 2θ at 27.6° and using λ_{ex} values of 53.4, 39.9, and 13.3 nm to obtain $L_{TG} = \lambda_{ex}/2\sin(\theta) = 110, 85,$ and 28 nm, respectively. The value of λ_{pr} was set to $\lambda_{ex}/3$ to fulfill the Bragg condition, except for data at $L_{TG} = 28$ nm, where $\lambda_{pr} = \lambda_{ex} = 13.3$ nm. In the latter configuration, the filtering at the detector was ineffective; however, the signal-to-noise ratio was still tolerable because the EUV TG signal was emitted at an angle, $\theta_{sig} = \sin^{-1}[\sin(\theta_{pr}) - \lambda_{pr}/L_{TG}] \approx -23.4^\circ$, far enough from the input trajectories of the excitation pulses (i.e., $\pm 13.8^\circ$). Furthermore, because this geometry does not fulfill the Bragg condition, the total signal is expected to decrease by a factor $\text{sinc}^2(\Delta k L_z/2)$, where $\Delta k = 2\pi[\cos(\theta_{sig}) - \cos(\theta_{pr})]/\lambda_{pr}$ is the wave vector mismatch and L_z is the

grating thickness. The latter can be regarded as the shorter length between the sample thickness (L_{sam}) and the absorption length of the pump ($L_{abs,ex}$).

Two different FEL settings were used to achieve the aforementioned conditions: (i) Data at $L_{TG} = 110$ nm were acquired using the FEL1 source with the fundamental emission at 53.4 nm (λ_{ex}), and the third harmonic content was enhanced by tuning one-third of the undulators to 17.8 nm (λ_{pr}); (ii) data corresponding to $L_{TG} = 85$ nm were acquired using the FEL2 source (17), with the first amplification stage tuned at 39.9 nm (λ_{ex}) and the second one at 13.3 nm (λ_{pr}). The conditions used to collect data at $L_{TG} = 28$ nm (i.e., $\lambda_{ex} = \lambda_{pr} = 13.3$ nm) were readily obtained from the latter FEL configuration by removing the SSFs from the pump branch lines and by inserting a Zr filter upstream of the whole system to cut the unnecessary radiation at 39.9 nm. In all settings, the polarization was linear vertical and the repetition rate was 50 Hz. The estimated FEL pulse duration is in the 40- to 70-fs range (shorter pulses at shorter wavelengths), substantially shorter than the observed dynamics. The seeding scheme adopted at the FERMI FEL allowed us to achieve almost Fourier transform-limited pulses and high stability in the output photon parameters, which were monitored on a shot-to-shot basis by a dedicated diagnostic system. The intensity fluctuations were on the 10% level, while the jitters in the central wavelength and pointing were well within the bandwidth and spot size at the sample, respectively.

The use of the FEL2 source allowed us to maximize the intensity of the probe radiation at the source, hence compensating for the lower throughput of the probe branch line, mainly due to the four multilayer mirrors in the DL. Typical intensities at the source (estimated intensities at the sample) for the pump/probe beams were 30/3 μJ (1/0.1 μJ) in the case of FEL1 source ($\lambda_{ex} = 53.4$ nm and $\lambda_{pr} = 17.8$ nm) and 25/40 μJ (2.5/2 μJ) in the case of FEL2 source ($\lambda_{ex} = 39.9$ nm and $\lambda_{pr} = 13.3$ nm); the estimated pump/probe intensity at the sample was about 10/1.5 μJ when $\lambda_{ex} = \lambda_{pr} = 13.3$ nm. The samples were Si₃N₄ membranes (Silson Ltd.) with thickness (50 nm) shorter than the absorption length at λ_{pr} (i.e., $L_{abs,pr} = 65/110$ nm at $\lambda_{pr} = 17.8/13.3$ nm) to mitigate the signal loss due to low sample transmission; the absorption length at $\lambda_{ex} = 53.4/39.9/13.3$ nm was $L_{abs,ex} = 10/17/110$ nm. The absorption length of the pump and probe radiation in Si (sample provided by Norcada) was 150 and 350 nm, respectively. The excitation energy density was in the 10/1 J/mm³ range for Si₃N₄/Si, and no sample damage was observed after prolonged (some hours) FEL exposure.

Data reduction

For each step in Δt , we acquired signal images (i.e., with all FEL beams ON) with an exposure time corresponding to 1000 to 3000 FEL shots (exposure time constant in a given scan). Background images (both pump ON/probe OFF and pump OFF/probe ON) with the same exposure time were collected every five Δt steps; a full scan lasted about 6 to 10 hours. Examples of signal, background, and background-subtracted images are shown in fig. S1B. The pump OFF/probe ON images also serve to check the eventual generation of a permanent grating on the sample surface. After background subtraction, we assumed that the EUV TG signal intensity was proportional to the total number of counts into the region of interest containing the signal beam (ROI_{sig}) minus those in a nearby region of interest (ROI_{prox}), where no signal was present. The counts were then normalized by the product of the relative intensities of the three input beams (with respect to the average intensity in the whole dataset), $I_{ex}^2(\Delta t)I_{pr}(\Delta t)/(\langle I_{ex}^2 \rangle \langle I_{pr} \rangle)$, and

converted into a number of photons by using the detector parameters (1 photon \approx 15/12 analog to digital units (ADU) counts at 13.3/17.8 nm) and accounting for the sample and filter transmission (in all configurations, a 150-nm-thick Zr filter was placed in front of the CCD detector). The values of $I_{\text{ex}}(\Delta t)$ and $I_{\text{pr}}(\Delta t)$ were determined by combining the information from the I0 monitor and EUV spectrometer in the photon diagnostic system upstream of the beamline; note that $I_{\text{ex}}(\Delta t) = I_{\text{pr}}(\Delta t)$ for the data at $L_{\text{TG}} = 28$ nm. This data reduction procedure results in a smoother waveform; however, the main features of the signal (i.e., the thermal decay and phonon modulations) are already evident from the raw signal, as shown in fig. S1D for the data at $L_{\text{TG}} = 85$ nm; similar results have been found in the other cases.

Error bar estimate

A rigorous determination of the error bars would require the acquisition of several data in identical conditions, which has not been possible in the present case because of the long acquisition time for a single waveform. However, a reasonable estimate can be provided by analyzing the scans where more than one signal image has been collected at each Δt step and those repeated more than one time in similar conditions, even if in a limited Δt range. This analysis is proposed in fig. S1E, from which one can infer an overall uncertainty of about 15%. This value is larger than the statistical error expected from the total ADU counts (typically $>10^3$) observed within ROI_{sig} and above the noise level (typically <0.1 photons/shot) estimated from the data at $\Delta t < 0$ (e.g., see Fig. 2D). This uncertainty could be due to jitters and drifts in the FEL pointing and/or other subtle parameters, for instance, the intensity distribution across the wavefront of the FEL beams, which cannot be accounted for by the data reduction procedure. However, it is worth noting that the “quality” of the present FEL pump/FEL probe data surpasses those from the few time-resolved experiments carried out on condensed matter by exclusively using FEL pulses. This highlights the great advantage of the “background-free conditions,” inherently related to the noncollinear wave-mixing approach used in the present work (and generally applicable also in other contexts).

Data analysis

To quantify the parameters characterizing the signal waveform, we used a basic data analysis, having the advantage of not relying upon specific modeling and consisting in an exponential function to estimate the slow decay (τ) and a Fourier transform to extract the oscillation frequency (ν). The TG signal intensity (I_{sig}) is quadratic with respect to the strain amplitude changes induced by the TG (4, 6, 18, 21, 22), and the thermoelastic response can be approximated by

$$I_{\text{sig}} \sim |A_{\text{th}} \exp(-\Delta t/\tau_{\text{th}}) + \sum_i A_i \exp(-\Delta t/\tau_i) \cos(2\pi\nu_i \Delta t)|^2 \quad (1)$$

where A_{th} and τ_{th} are the amplitude and time decay of the thermal relaxation, respectively, while A_i and τ_i are those of the coherent phonon excitations. Therefore, the exponential decay of the signal is characterized by a time constant $\tau_{\text{th}}/2$ (red lines in Fig. 2), while the decay rate of the ν_i modulations, $\tau_{\text{th}}^{-1} + \tau_i^{-1}$, is determined by both the thermal and phonon decay. Consequently, the oscillations at ν_i in the signal appear as damped even if the coherent phonon excitations do not decay at all in the probed time scale. This is the expected situation for both samples, because the time decay of LA phonons is expected to be about one order of magnitude longer than τ_{th} (38). According to Eq. 1, the signal should

also contain components oscillating at $2\nu_i$, with decay rates of $2/\tau_i$, that would persist beyond the thermal relaxation. We investigated this behavior in our previous experiment with an optical probe (18); however, in the present study, our measurements lack a sufficient range in Δt and signal-to-noise ratio for determining the $2\nu_i$ oscillating term. We estimated τ_{th} from the best fit of the data to Eq. 1 with $A_i = 0$ (red lines in Figs. 2, A to C, and 4), which resulted, respectively, in $\tau_{\text{th}} = 750 \pm 190$ ps, 370 ± 50 ps, and 42 ± 9 ps for $L_{\text{TG}} = 110$, 85, and 28 nm (for Si_3N_4) and in $\tau_{\text{th}} = 73 \pm 12$ ps for Si at $L_{\text{TG}} = 110$ nm. The value of the thermal diffusivity, $D_{\text{th}} = 470 \pm 90$ nm²/ns, estimated from data in Fig. 3B, is in the range of the values reported in the literature (24). However, we have to notice that the thermal properties of Si_3N_4 membranes show large variations, even in samples from the same batch (24, 35, 39, 40). For instance, values as different as 500 nm²/ns (24) and 2500 nm²/ns (40) were reported for different fabrication procedures, compositions, residual stress, thickness, etc.

After subtraction of the corresponding $A_{\text{th}} \exp\{-2\Delta t/\tau_{\text{th}}\}$ terms from the signal, the residual waveforms are Fourier-transformed to determine their spectral content (the results are shown in fig. S1F). The main peak matches the frequency expected for LA phonons, as discussed in the main text (see Fig. 3A), while weaker peaks at low frequencies and at 2ν can be perceived above the noise level. However, higher quality data and an extended Δt range are needed to investigate these features.

SUPPLEMENTARY MATERIALS

Supplementary material for this article is available at <http://advances.sciencemag.org/cgi/content/full/5/7/eaaw5805/DC1>

Fig. S1. Experimental details.

REFERENCES AND NOTES

1. T. E. Glover, D. M. Fritz, M. Cammarata, T. K. Allison, S. Coh, J. M. Feldkamp, H. Lemke, D. Zhu, Y. Feng, R. N. Coffee, M. Fuchs, S. Ghimire, J. Chen, S. Schwartz, D. A. Reis, S. E. Harris, J. B. Hastings, X-ray and optical wave mixing. *Nature* **488**, 603–608 (2012).
2. R. K. Lam, S. L. Raj, T. A. Pascal, C. D. Pemmaraju, L. Foglia, A. Simoncig, N. Fabris, P. Miotti, C. J. Hull, A. M. Rizzuto, J. W. Smith, R. Mincigrucci, C. Masciovecchio, A. Gessini, E. Allaria, G. De Ninno, B. Diviacco, E. Roussel, S. Spampinati, G. Penco, S. Di Mitri, M. Trovò, M. Danailov, S. T. Christensen, D. Sokaras, T.-C. C. Weng, M. Coreno, L. Poletto, W. S. Drisdell, D. Prendergast, L. Giannessi, E. Principi, D. Nordlund, R. J. Saykally, C. P. Schwartz, Soft X-ray second harmonic generation as an interfacial probe. *Phys. Rev. Lett.* **120**, 23901 (2018).
3. M. Fuchs, M. Trigo, J. Chen, S. Ghimire, S. Schwartz, M. Kozina, M. Jiang, T. Henighan, C. Bray, G. Ndabashimiye, P. H. Bucksbaum, Y. Feng, S. Herrmann, G. A. Carini, J. Pines, P. Hart, C. Kenney, S. Guillet, S. Boutet, G. J. Williams, M. Messerschmidt, M. M. Seibert, S. Moeller, J. B. Hastings, D. A. Reis, Anomalous nonlinear X-ray Compton scattering. *Nat. Phys.* **11**, 964–970 (2015).
4. F. Bencivenga, R. Cucini, F. Capotondi, A. Battistoni, R. Mincigrucci, E. Giangrisostomi, A. Gessini, M. Manfreda, I. P. P. Nikolov, E. Pedersoli, E. Principi, C. Svetina, P. Parisse, F. Casolari, M. B. Danailov, M. Kiskinova, C. Masciovecchio, Four-wave mixing experiments with extreme ultraviolet transient gratings. *Nature* **520**, 205–208 (2015).
5. K. A. Nelson, R. J. D. Miller, D. R. Lutz, M. D. Fayer, Optical generation of tunable ultrasonic waves. *J. Appl. Phys.* **53**, 1144–1149 (1982).
6. N. Boechler, J. K. Eliason, A. Kumar, A. A. Maznev, K. A. Nelson, N. Fang, Interaction of a contact resonance of microspheres with surface acoustic waves. *Phys. Rev. Lett.* **111**, 036103 (2013).
7. J. Goldshteyn, A. Bojahr, P. Gaal, D. Schick, M. Bargheer, Selective preparation and detection of phonon polariton wavepackets by stimulated Raman scattering. *Phys. Status Solidi B Basic Res.* **251**, 821–828 (2014).
8. J. A. Johnson, A. A. Maznev, J. Cuffe, J. K. Eliason, A. J. Minnich, T. Kehoe, C. M. S. Torres, G. Chen, K. A. Nelson, Direct measurement of room-temperature nondiffusive thermal transport over micron distances in a silicon membrane. *Phys. Rev. Lett.* **110**, 025901 (2013).

9. N. K. Ravichandran, H. Zhang, A. J. Minnich, Spectrally resolved specular reflections of thermal phonons from atomically rough surfaces. *Phys. Rev. X* **8**, 041004 (2018).
10. S. Tang, M. Wang, B. D. Olsen, Anomalous self-diffusion and sticky Rouse dynamics in associative protein hydrogels. *J. Am. Chem. Soc.* **137**, 3946–3957 (2015).
11. N. Osada, T. Oshima, S. Kuwahara, T. Toyoda, Q. Shen, K. Katayama, Photoexcited carrier dynamics of double-layered CdS/CdSe quantum dot sensitized solar cells measured by heterodyne transient grating and transient absorption methods. *Phys. Chem. Chem. Phys.* **16**, 5774–5778 (2014).
12. L. Yang, J. D. Koralek, J. Orenstein, D. R. Tibbetts, J. L. Reno, M. P. Lilly, Coherent propagation of spin helices in a quantum-well confined electron gas. *Phys. Rev. Lett.* **109**, 246603 (2012).
13. C. S. Davies, J. Janušonis, A. V. Kimel, A. Kirilyuk, A. Tsukamoto, T. Rasing, R. I. Tobey, Towards massively parallelized all-optical magnetic recording. *J. Appl. Phys.* **123**, 213904 (2018).
14. D. H. Torchinsky, F. Mahmood, A. T. Bollinger, I. Božović, N. Gedik, Fluctuating charge-density waves in a cuprate superconductor. *Nat. Mater.* **12**, 387–391 (2013).
15. A. Leblanc, A. Deneud, L. Chopineau, G. Mennerat, P. Martin, F. Quéré, Plasma holograms for ultrahigh-intensity optics. *Nat. Phys.* **13**, 440–443 (2017).
16. K. Kuroi, K. Okajima, M. Ikeuchi, S. Tokutomi, M. Terazima, Transient conformational fluctuation of TePixD during a reaction. *Proc. Natl. Acad. Sci. U.S.A.* **111**, 14764–14769 (2014).
17. E. Allaria, D. Castronovo, P. Cinquegrana, P. Craievich, M. Dal Forno, M. B. Danilov, G. D'Auria, A. Demidovich, G. De Ninno, S. Di Mitri, B. Diviacco, W. M. Fawley, M. Ferianis, E. Ferrari, L. Froehlich, G. Gaio, D. Gauthier, L. Giannessi, R. Ivanov, B. Mahieu, N. Mahne, I. Nikolov, F. Parmigiani, G. Penco, L. Raimondi, C. Scafuri, C. Serpico, P. Sigalotti, S. Spampinati, C. Spezzani, M. Svandrlík, C. Svetina, M. Trovo, M. Veronese, D. Zangrando, M. Zangrando, Two-stage seeded soft-X-ray free-electron laser. *Nat. Photonics* **7**, 913–918 (2013).
18. A. A. Maznev, F. Bencivenga, A. Cannizzo, F. Capotondi, R. Cucini, R. A. Duncan, T. Feurer, T. D. Frazer, F. Foglia, H.-M. Frey, H. Kapteyn, J. Knobloch, G. Knopp, C. Masciovecchio, R. Mincigrucci, G. Monaco, M. Murnane, I. Nikolov, E. Pedersoli, A. Simoncig, A. Vega-Flick, K. A. Nelson, Generation of coherent phonons by coherent extreme ultraviolet radiation in a transient grating experiment. *Appl. Phys. Lett.* **113**, 221905 (2018).
19. L. Foglia, F. Capotondi, R. Mincigrucci, D. Naumenko, E. Pedersoli, A. Simoncig, G. Kurdi, A. Calvi, M. Manfreda, L. Raimondi, N. Mahne, M. Zangrando, C. Masciovecchio, F. Bencivenga, First evidence of purely extreme-ultraviolet four-wave mixing. *Phys. Rev. Lett.* **120**, 263901 (2018).
20. R. Mincigrucci, L. Foglia, D. Naumenko, E. Pedersoli, A. Simoncig, R. Cucini, A. Gessini, M. Kiskinova, G. Kurdi, N. Mahne, M. Manfreda, I. P. Nikolov, E. Principi, L. Raimondi, M. Zangrando, C. Masciovecchio, F. Capotondi, F. Bencivenga, Advances in instrumentation for FEL-based four-wave-mixing experiments. *Nucl. Instrum. Methods Phys. Res.* **907**, 132–148 (2018).
21. H. J. Eichler, P. Günter, D. Pohl, *Laser-Induced Dynamic Gratings* (Springer-Verlag, 1986).
22. R. I. Tobey, M. E. Siemens, O. Cohen, M. M. Murnane, H. C. Kapteyn, K. A. Nelson, Ultrafast extreme ultraviolet holography: Dynamic monitoring of surface deformation. *Opt. Lett.* **32**, 286–288 (2007).
23. A. Khan, J. Philip, P. Hess, Young's modulus of silicon nitride used in scanning force microscope cantilevers. *J. Appl. Phys.* **95**, 1667–1672 (2004).
24. S.-M. Lee, D. G. Cahill, Heat transport in thin dielectric films. *J. Appl. Phys.* **81**, 2590–2595 (1997).
25. S. Ruhman, L. R. Williams, A. G. Joly, B. Kohler, K. A. Nelson, Nonrelaxational inertial motion in CS₂ liquid observed by femtosecond time-resolved impulsive stimulated scattering. *J. Phys. Chem.* **91**, 2237–2240 (1987).
26. Y. Shvyd'ko, S. Stoupin, D. Shu, S. P. Collins, K. Mundboth, J. Sutter, M. Tolkiehn, High-contrast sub-millivolt inelastic X-ray scattering for nano- and mesoscale science. *Nat. Commun.* **5**, 4219 (2014).
27. F. Bencivenga, C. Masciovecchio, FEL-based transient grating spectroscopy to investigate nanoscale dynamics. *Nucl. Instrum. Methods Phys. Res.* **606**, 785–789 (2009).
28. C. Ferrante, E. Pontecorvo, G. Cerullo, A. Chiasera, G. Ruocco, W. Schirmacher, T. Scopigno, Acoustic dynamics of network-forming glasses at mesoscopic wavelengths. *Nat. Commun.* **4**, 1793 (2013).
29. G. Monaco, S. Mossa, Anomalous properties of the acoustic excitations in glasses at the mesoscopic length scale. *Proc. Natl. Acad. Sci. U.S.A.* **106**, 16907–16912 (2009).
30. F. Mallamace, C. Corsaro, H. E. Stanley, Possible relation of water structural relaxation to water anomalies. *Proc. Natl. Acad. Sci. U.S.A.* **110**, 4899–4904 (2013).
31. A. J. McKenna, J. K. Eliason, D. J. Flannigan, Spatiotemporal Evolution of Coherent Elastic Strain Waves in a Single MoS₂ Flake. *Nano Lett.* **17**, 3952–3958 (2017).
32. A. Feist, N. Rubiano da Silva, W. Liang, C. Ropers, S. Schäfer, Nanoscale diffractive probing of strain dynamics in ultrafast transmission electron microscopy. *Struct. Dyn.* **5**, 014302 (2018).
33. K. M. Hoogeboom-Pot, J. N. Hernandez-Charpak, X. Gu, T. D. Frazer, E. H. Anderson, W. Chao, R. W. Falcone, R. Yang, M. M. Murnane, H. C. Kapteyn, D. Nardi, A new regime of nanoscale thermal transport: Collective diffusion increases dissipation efficiency. *Proc. Natl. Acad. Sci. U.S.A.* **112**, 4846–4851 (2015).
34. Y. Hu, L. Zeng, A. J. Minnich, M. S. Dresselhaus, G. Chen, Spectral mapping of thermal conductivity through nanoscale ballistic transport. *Nat. Nanotechnol.* **10**, 701–706 (2015).
35. R. Sultan, A. D. Avery, J. M. Underwood, S. J. Mason, D. Bassett, B. L. Zink, Heat transport by long mean free path vibrations in amorphous silicon nitride near room temperature. *Phys. Rev. B* **87**, 214305 (2013).
36. A. Eschenlohr, M. Battiatto, P. Maldonado, N. Pontius, T. Kachel, K. Holldack, R. Mitzner, A. Föhlisch, P. M. Oppeneer, C. Stamm, Ultrafast spin transport as key to femtosecond demagnetization. *Nat. Mater.* **12**, 332–336 (2013).
37. S. Tanaka, S. Mukamel, X-ray four-wave mixing in molecules. *J. Chem. Phys.* **116**, 1877–1891 (2002).
38. P. Emery, A. Devos, Acoustic attenuation measurements in transparent materials in the hypersonic range by picosecond ultrasonics Acoustic attenuation measurements in transparent materials in the hypersonic range by picosecond ultrasonics. *Appl. Phys. Lett.* **89**, 191904 (2015).
39. H. Ftouni, C. Blanc, D. Tainoff, A. D. Fefferman, M. Defoort, K. J. Lulla, J. Richard, E. Collin, O. Bourgeois, Thermal conductivity of silicon nitride membranes is not sensitive to stress. *Phys. Rev. B Condens. Matter Mater. Phys.* **92**, 125439 (2015).
40. A. Jain, K. E. Goodson, Measurement of the thermal conductivity and heat capacity of freestanding shape memory thin films using the 3ω method. *J. Heat Transf.* **130**, 102402 (2008).

Acknowledgments: We gratefully acknowledge M. Kiskinova, M. Svandrlík, and the FERMI team for their support throughout the whole project. **Funding:** We gratefully acknowledge financial support from the European Research Council through grant N.202804-TIMER. The contribution of the MIT group was supported by the U.S. Department of Energy, Office of Science, Office of Basic Energy Sciences, under Award DE-SC0001299; Solid-State Solar-Thermal Energy Conversion Center (S³TEC); Energy Frontier Research Center; and Award DE-SC0019126. M.Ma. and H.K. gratefully acknowledge support from a Gordon and Betty Moore Foundation EPIQS Award through grant GBMF4538 and from the Department of Energy BES Award No. DE-FG02-99ER14982. J.K. gratefully acknowledges support from an SRC Graduate Fellowship. **Author contributions:** C.M. proposed the FEL-based TG approach and provided guidance throughout the whole process. F.B. designed the experimental setup and coordinated its realization. F.B., R.M., F.Capot., L.F., D.N., E.Pe., A.S., R.C., G.G., A.G., G.K., N.M., M.Ma., E.Pr., L.R., and M.Z. commissioned the instrument. F.B., A.A.M., G.C., H.K., G.M., M.Mu., K.A.N., and C.M. proposed the experiment. F.B., R.M., F.Capot., L.F., D.N., A.A.M., E.Pe., A.S., F.Capor., V.C., F.D., R.A.D., T.D.F., S.H., J.K., A.M., and G.M. carried out the measurements. G.G., A.G., L.G., G.K., N.M., M.Ma., L.R., S.S., C.S., M.T., and M.Z. set up the FEL machine, the photon transport system, and timing diagnostics. F.B., R.M., and F.Capot. analyzed the data. F.B., R.M., F.Capot., L.F., A.A.M., and C.M. wrote the paper with contributions from other authors. **Competing interests:** The authors declare that they have no competing interests. **Data and materials availability:** All data needed to evaluate the conclusions in the paper are present in the paper and/or the Supplementary Materials. Additional data related to this paper may be requested from the authors.

Submitted 7 January 2019

Accepted 20 June 2019

Published 26 July 2019

10.1126/sciadv.aaw5805

Citation: F. Bencivenga, R. Mincigrucci, F. Capotondi, L. Foglia, D. Naumenko, A. A. Maznev, E. Pedersoli, A. Simoncig, F. Caporaletti, V. Chiloyan, R. Cucini, F. Dallari, R. A. Duncan, T. D. Frazer, G. Gaio, A. Gessini, L. Giannessi, S. Huberman, H. Kapteyn, J. Knobloch, G. Kurdi, N. Mahne, M. Manfreda, A. Martinelli, M. Murnane, E. Principi, L. Raimondi, S. Spampinati, C. Spezzani, M. Trovo, M. Zangrando, G. Chen, G. Monaco, K. A. Nelson, C. Masciovecchio, Nanoscale transient gratings excited and probed by extreme ultraviolet femtosecond pulses. *Sci. Adv.* **5**, eaaw5805 (2019).

Nanoscale transient gratings excited and probed by extreme ultraviolet femtosecond pulses

F. Bencivenga, R. Mincigrucci, F. Capotondi, L. Foglia, D. Naumenko, A. A. Maznev, E. Pedersoli, A. Simoncig, F. Caporaletti, V. Chiloyan, R. Cucini, F. Dallari, R. A. Duncan, T. D. Frazer, G. Gaio, A. Gessini, L. Giannessi, S. Huberman, H. Kapteyn, J. Knobloch, G. Kurdi, N. Mahne, M. Manfredda, A. Martinelli, M. Murnane, E. Principi, L. Raimondi, S. Spampinati, C. Spezzani, M. Trovò, M. Zangrando, G. Chen, G. Monaco, K. A. Nelson and C. Masciovecchio

Sci Adv 5 (7), eaaw5805.
DOI: 10.1126/sciadv.aaw5805

ARTICLE TOOLS

<http://advances.sciencemag.org/content/5/7/eaaw5805>

SUPPLEMENTARY MATERIALS

<http://advances.sciencemag.org/content/suppl/2019/07/22/5.7.eaaw5805.DC1>

REFERENCES

This article cites 39 articles, 4 of which you can access for free
<http://advances.sciencemag.org/content/5/7/eaaw5805#BIBL>

PERMISSIONS

<http://www.sciencemag.org/help/reprints-and-permissions>

Use of this article is subject to the [Terms of Service](#)

Science Advances (ISSN 2375-2548) is published by the American Association for the Advancement of Science, 1200 New York Avenue NW, Washington, DC 20005. The title *Science Advances* is a registered trademark of AAAS.

Copyright © 2019 The Authors, some rights reserved; exclusive licensee American Association for the Advancement of Science. No claim to original U.S. Government Works. Distributed under a Creative Commons Attribution NonCommercial License 4.0 (CC BY-NC).